Research Article

Corrosion mechanisms of Zr-based bulk metallic glass in NaF and NaCl solutions

Zhangweijia Qiu [a,b], Zhengkun Li [b], Huameng Fu [b,d,*], Hongwei Zhang [b,c,d], Zhengwang Zhu [b,d], Aimin Wang [b,d], Hong Li [b], Long Zhang [b], Haifeng Zhang [b,d,*]

[a] School of Materials Science and Engineering, University of Science and Technology of China, Shenyang 110016, China
[b] Shenyang National Laboratory for Material Science, Institute of Metal Research, Chinese Academy of Sciences, Shenyang 110016, China
[c] Shenyang Amorphous Metal Manufacturing Co., Ltd, Shenyang 110000, China
[d] Dongguan Eontec Co., Ltd, Dongguan 523662, China

ARTICLE INFO

ABSTRACT

So far, some investigations related to the corrosion mechanism of Zr-based metallic glasses in solutions containing Cl⁻ have been developed. However, few attentions have been paid to the situation in F⁻-containing solution. This paper describes the corrosion behaviours of $Zr_{52}Al_{10}Ni_6Cu_{32}$ bulk metallic glass (BMG) in NaF and NaCl aqueous solutions. The corrosion mechanism of Zr-based BMG in F–containing solution was proposed for the first time. It was found that in NaCl solutions, Zr-based BMG samples underwent typical pitting corrosion. Selective dissolution of Zr, Al and enrichment of Cu were observed in corrosion pits. However, corrosion occurred in the form of general breakdown of passive film in NaF solutions. Such difference is interpreted in terms of the binding ability of anions to surrounding molecules, i.e., Cl⁻ with loose surrounding water passes through the passive film to cause pitting; F⁻ with a tight surrounding molecules layer absorbs on passive film then coordinates with cations from matrix.

© 2020 Published by Elsevier Ltd on behalf of The editorial office of Journal of Materials Science & Technology.

1. Introduction

Metallic glass has been extensively studied from different perspectives over the past few decades. The research aspects include glass-forming ability [1,2], structure [3], mechanical properties [4–6], corrosion resistance [7,8] and recently catalytic performance [9,10]. Owing to the good glass-forming ability, high mechanical strength and low Young's modulus, Zr-based bulk metal glasses (BMGs) are considered to be promising materials for various applications [11,12]. Also, compared to their crystalline counterpart Zr-based BMG materials exhibit the advantage of high corrosion resistance which is attributed to their componential and structural homogeneity and lack of lattice defects. For example, Zr-based BMGs show extremely low corrosion current density and wide passivation range in sulphate and hydroxide solutions. However, they are susceptible to pitting corrosion in the presence of chloride ions [13–15]. It has been found that Zr-based BMGs normally form a protective passive film mainly comprised of Zr oxides, which is

similar to the corrosion behaviour of pure zirconium [16–18]. In Cl⁻-containing solutions, preferential dissolution of Zr and Al is often observed, resulting in Cu enrichment in pit region [19,20]. The sensitivity of metallic glasses to pitting corrosion is due to crystalline inclusions and structural imperfections during fabrication process [13,16,21]. Various technical approaches have been developed to improve the corrosion resistance of Zr-based BMG materials in Cl⁻-containing solutions, such as alloy composition modification [22–24], surface coating by PVD method [25].

The potential of Zr-based bulk metallic glasses as biomaterials has been confirmed for their bio-compatibility and high chemical stability in the human body. As a good candidate of bone fracture fixation or dental implants, Zr-based bulk metallic glasses may encounter ions including SO_4^{2-}, Cl- and F- in solution [26,27]. Thus, to understand the corrosion resistance of these materials in solution with different ions is becoming more crucial for the efforts to broaden their service environments. Although quantities of research have been reported on corrosion resistance of Zr-based metallic glasses in Cl–containing solutions, few have been developed for F–containing solutions. There are some studies mainly about the corrosion of Zr-based metallic glass in hydrofluoric acid (HF) under free corrosion [28–30]. But they deviate from the corrosion in aqueous solution under normal conditions.

* Corresponding authors at: Shenyang National Laboratory for Material Science, Institute of Metal Research, Chinese Academy of Sciences, Shenyang 110016, China.
E-mail addresses: hmfu@imr.ac.cn (H. Fu), hfzhang@imr.ac.cn (H. Zhang).

With the highest electronegativity and the minimum ion radius, fluorine is supposed to be the most corrosive halogen element to alloys. However, it has been found that the dissolution rate of zirconium in Cl^--containing solutions is higher than that in F^--containing solutions [31,32]. Furthermore, it is also a controversy that whether the alloys are pitted or uniformly corroded in F–containing solution. Duan et al. [33] proposed that the corrosion mechanism of the Pb-based alloys in NaF and NaI solutions is localized corrosion versus mainly general corrosion in NaCl and NaBr solutions, and the corrosion resistance of alloys to F^- is higher than that to Cl^-. In addition, Davies et al. [34] found that the pitting potentials of Al in Cl^--containing solutions are lower than the pitting potentials in F^--containing solutions. Nevertheless, Trompette et al. [35–38] conducted a series of studies on the effect of cations' cosmotrope/chaotrope nature on corrosion behaviour of Al, Ti, Fe and Sn. For these metals, pitting was observed in Cl^--containing solutions, but not in F^--containing solutions. These experimental results indicate that the mechanism of passive film breakdown occurred in the F^--containing solution is still ambiguous.

Apparently, developing research in this field will bebeneficial to understand the corrosion behaviours of BMG materials in F^--containing environment. For the purpose, in this paper we comparatively studied the corrosion behaviours of $Zr_{52}Al_{10}Ni_6Cu_{32}$ metallic glass in NaF and NaCl solutions. Standard electrochemical methods were applied to inspect and to measure the corrosion resistance of the material. The structure and composition of the corroded surface were also characterized, and the possible corrosion mechanisms were proposed and discussed in detail.

2. Experimental

2.1. Sample preparation

The nominal composition of the Zr-based BMG is $Zr_{52}Al_{10}Ni_6Cu_{32}$ (at.%). The ingots of highly pure Zr, Cu, Al, and Ni (>99.8 wt.%) were prepared by arc melting under Ti-gettered argon atmosphere. In order to ensure the homogeneity of composition, all ingots were remelted for at least four times. Rods of metallic glass with 3 mm in diameter were then produced by injection copper mold casting in high-purity argon atmosphere. BMG rods as working electrode was electrically connected with copper wires, and then sealed in epoxy resin with an exposed area of 0.071 cm^2. Before electrochemical studies, the samples were polished with sandpaper from 400 grit to 5000 grit then polished with $1.0 \mu m$ grinding paste in deionized water, degreased in acetone and finally dried in air. The thin foils for TEM experiments were prepared via a standard twin-jet electropolishing with an electrolyte of perchloric acid (6 vol.%), butyl alcohol (35 vol.%) and methanol (59 vol.%) at 253 K.

2.2. Electrochemical tests

The solutions were prepared from analytical grade sodium fluoride (NaF), sodium chloride (NaCl) and deionized water. The pH values of the solutions were measured with an electronic pH-meter (LICHEN pH-100A) before electrochemical experiments. The pH values of 0.1 M NaCl solutions were about 6.5 ± 0.1 and approximately 8.2 in 0.1 M NaF solutions. The reason for the deviation of the pH value from 7.0 at 298 K for NaCl solution is that carbon dioxide (CO_2) in air dissolves in water then form carbonic acid. On the other hand, fluoride can develop a strong electrostatic attraction with hydrogen ions (H^+), which leads to an increase in pH value. To eliminate the influence of pH, some droplets of diluted hydrofluoric acid (HF) solution or NaOH solution were added to ensure that pH value of all solutions used is about 7.0 ± 0.1.

All electrochemical tests were performed using a Gamry Interface1000 electrochemical workstation at 298 K. The electrochemical cell contained a platinum foil as counter electrode and a saturated calomel electrode (SCE) as reference electrode. The open circuit potential (OCP) was monitored for 90 min after sample immersion, then electrochemical impedance spectroscopy (EIS) data was acquired from 100 kHz to 100 mHz with potential amplitude of 10 mV. ZSimpWin software was used for analysis of the EIS spectra. Then potentiodynamic polarization was also recorded at a potential sweep rate of 0.167 mV/s after OCP tests. Electrochemical parameters were obtained using Gamry Echem Analyst software. Each test was repeated four times to ensure the results are reproducible. After electrochemical tests, the samples were cleaned with acetone then dried in air.

2.3. Surface analysis

The corrosion morphologies of alloy surface were examined by SEM (Zeiss supra 55), The surface microstructure and composition were characterized by XRD (Rigaku D/max 2400 diffractometer with Cu Kα radiation) and TEM (FEI F20, Tecnai T12). XPS (ESCALAB250 with Al K_α of 1486.6 eV) was also used for better understanding surface structures.
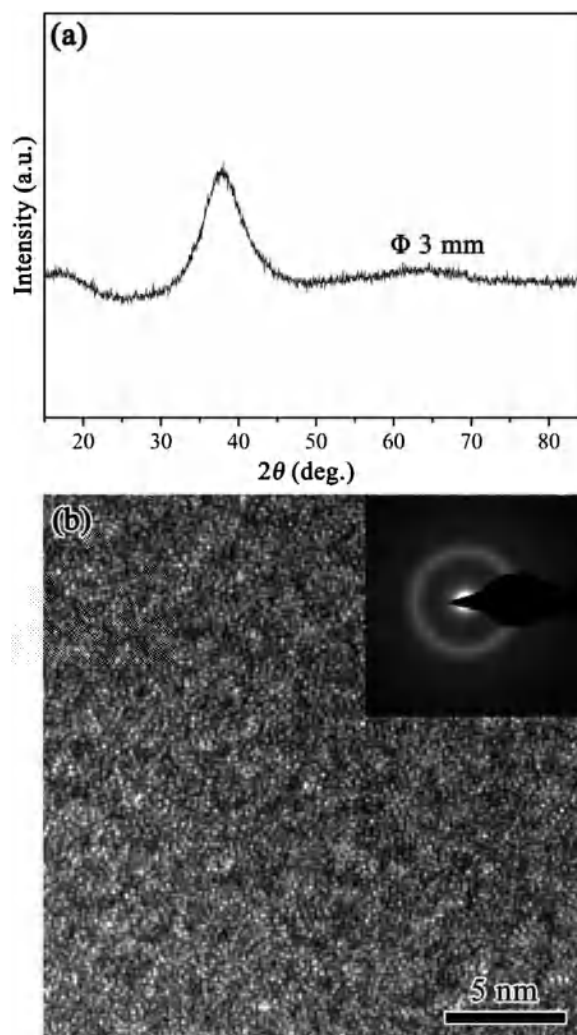
Fig. 1. Microstructure characterizations for as-cast $Zr_{52}Al_{10}Ni_6Cu_{32}$ BMG sample: (a) XRD pattern; (b) HRTEM image with the corresponding SAED pattern in the inset.

3. Results

3.1. Structure characterization

Fig. 1(a) shows the XRD pattern of as-cast rod samples of 3 mm in diameters. The XRD pattern of as-cast sample exhibit a broad diffuse halo without obvious sharp peaks on the curve, indicating the sample is fully amorphous. Fig. 1(b) presents the HRTEM image of the as-cast 3 mm sample which shows a homogeneous contrast without long-term periodically ordered feature. The corresponding SAED pattern confirms the glassy nature of the sample.

3.2. Free corrosion condition

Fig. 2 shows the trend of open circuit potential of Zr-based metallic samples in NaF and NaCl solution with time and the results of subsequent EIS experiments. It can be seen from Fig. 2(a) and (b) that OCP increases in NaCl solution and decreases in NaF solution. The OCPs finally become steady (variation less than 1 mV/min), which means the alloy surface has reached quasi-steady-state. The increase and decrease in OCP over time are generally attributed to the formation and destruction of passive film, respectively [39–41]. The final value, i.e., the value of OCP at the end of measurement (5400 s in Fig. 2, decreases with the addition of NaCl/NaF, which indicates the stability of passive film is further damaged with increasing Cl^-/F^-.

Fig. 2(c) and (d) provide the EIS results in the NaCl/NaF solutions as Nyquist plots, the corresponding electrical equivalent circuits (EEC) for fitting data are also presented. The electrochemical parameters obtained by fitting are shown in Table 1. It is worth noting that the constant phase elements (CPE) substitution of pure capacitance here is due to the distribution of relaxation times which originates from the surface roughness and inhomogeneity [42,43]. The impedance of CPE is defined by the following formula.

$$Z_{CPE} = \frac{1}{Q} \cdot \frac{1}{(jw)^n} \tag{1}$$

The values of n range between 0 and 1. When $n = 1$, CPE exhibits the properties of ideal capacitor. When $n = 0$, CPE becomes an ideal resistance. For the situation in NaCl solution (Fig. 2(c)), all curves exhibit a single capacitive loop with similar radii. The EEC for fitting includes: R_s, the resistance of the solution between the reference electrode and the working electrode; CPE represents the double layer capacitance; R_f is the resistance of passive film, which is directly associated with the rate of charge transfer. Values of n in NaCl solution are approximately 0.9, which suggests that the double layer has deviated from the ideal capacitance behaviour. All R_f values are on the order of 10^5 $\Omega \cdot cm^2$, demonstrating the good protection of the passive film formed in NaCl solution.

However, in the case of NaF solution (Fig. 2(d)), the radius of the capacitive loop decreases with the increase of NaF concentration. Accordingly, the EEC in Fig. 2(c) cannot achieve satisfactory agreement (χ^2 in the order of 10^{-2}). Therefore, the EEC in Fig. 2(d) was proposed for fitting. The physical meanings of this equivalent circuit are various. Some authors interpreted this EEC as a defect containing passive film formed on the surface of alloys [44,45]. The values of χ^2 in the order of 10^{-4} shown in Table 1 also indicate a good agreement between the experimental and fitted data. Here, CPE_1 and CPE_2 correspond to the capacitance of outer film and inner film, R_{f1} and R_{f2} characterize the resistance of the defect containing film and the interface between alloy and solution, respectively. The R_f value in NaCl solution remains almost unchanged with Cl-concentration. By contrast, the values of R_{f1} and R_{f2} both decreased with NaF concentration in solution. An advantage of EIS is that the electrochemical parameter R_p can be measured, which is directly related to corrosion resistance [46]. R_p is defined as $R_p = Z_{F(w=0)}$-

$Z_{F(w=\infty)}$, and it can also be calculated by $R_{f1} + R_{f2}$, which are listed in Table 1. By comparing the R_p values in the two solutions, we can see that the corrosion resistance in NaF solution decreases rapidly with the solute concentration. Whereas in NaCl solution, the R_p values are remained on the order of 10^5 $\Omega \cdot cm^2$ and only decreased slowly with the increase of solute.

Fig. 3 gives the typical SEM images of the surface of $Zr_{52}Al_{10}Ni_6Cu_{32}$ metallic glass after OCP tests. The SEM graphs related to 0.05 M and 0.1 M solutions are not displayed due to the lack of characteristic morphology of corrosion. Fig. 3(a and b) show the corrosion morphology of Zr-based metallic glass after immersion in 0.2 M and 0.5 M NaCl solutions. Obviously, corrosion pits only appear in the sample immersed in 0.5 M NaCl solution, which is the typical corrosion morphology feature for metallic glass in Cl^- containing solution. Except for corrosion pits, no further corrosion phenomenon can be seen in the overall morphology of the sample. Furhermore, Fig. 3(c and d) reveal that the corrosion morphologies in 0.2 M and 0.5 M NaF solutions are completely different from those in NaCl solutions. Sample surface scratches and defects caused by mechanical polishing disappeared during the corrosion process. Granular corrosion products can be observed on the sample surface. As the concentration of the NaF changes from 0.2 M to 0.5 M, the particle size of the corrosion product increases. These corrosion morphology characteristics make known that the Zr-based metallic glass is uniformly corroded in NaF solution under free corrosion condition.

3.3. Polarization behaviour

The representative polarization curves of Zr-based BMG measured in the NaCl and NaF solutions are compared in Fig. 4. As can be seen from Fig. 4(a), pitting occurred in NaCl solutions. On the polarization curves, a sharp increase by several orders of magnitude within seconds in the current density occurs when potential reaches a certain value, this specific potential is defined as E_{pit} (pitting potential) [47,48]. After pitting occurs, the current density rapidly reaches the order of 10^5 $\mu A/cm^2$, and then enters the diffusion-controlled region. Fig. 4(b) shows that in F^--containing solution, Zr-based BMG exhibits different corrosion behaviours. Although these curves also have inflection points, they are not as clear as those in NaCl solutions. Furthermore, the dense data points observed in the rising part of the curve indicate that the current does not increase suddenly during the corrosion process, thus the breakdown mechanism of the passive film may not be pitting corrosion. The current controlled by diffusion eventually reached an order of 10^3 $\mu A/cm^2$. In order to compare with the results obtained in NaCl solution, we define the voltage at this inflection point as E_b (breakdown potential), which is the level where the destruction of passive film occurs.

Table 2 lists the electrochemical parameters derived from the polarization curves. It can be seen that the corrosion potential (E_{corr}), E_{pit} and E_b decreased with the increase of concentration, which is consistent with the results of the OCP test. Although at the same solute concentration, the E_b in NaF solution was higher than the E_{pit} in NaCl solution, the corrosion current in NaF solution was higher than in NaCl solution, which suggests that the NaF solution is more detrimental than NaCl solution under free corrosion condition. In addition, as previously mentioned, the diffusion current in NaF solution is two orders of magnitude lower than that in NaCl solution, so it is reasonable to speculate that a diffusion barrier layer was formed on the surface of the alloy in NaF solution.

3.4. Morphology of corroded surface

Fig. 5 shows the morphology of $Zr_{52}Al_{10}Ni_6Cu_{32}$ BMG samples after pitting and corresponding EDS results for highlighted area A
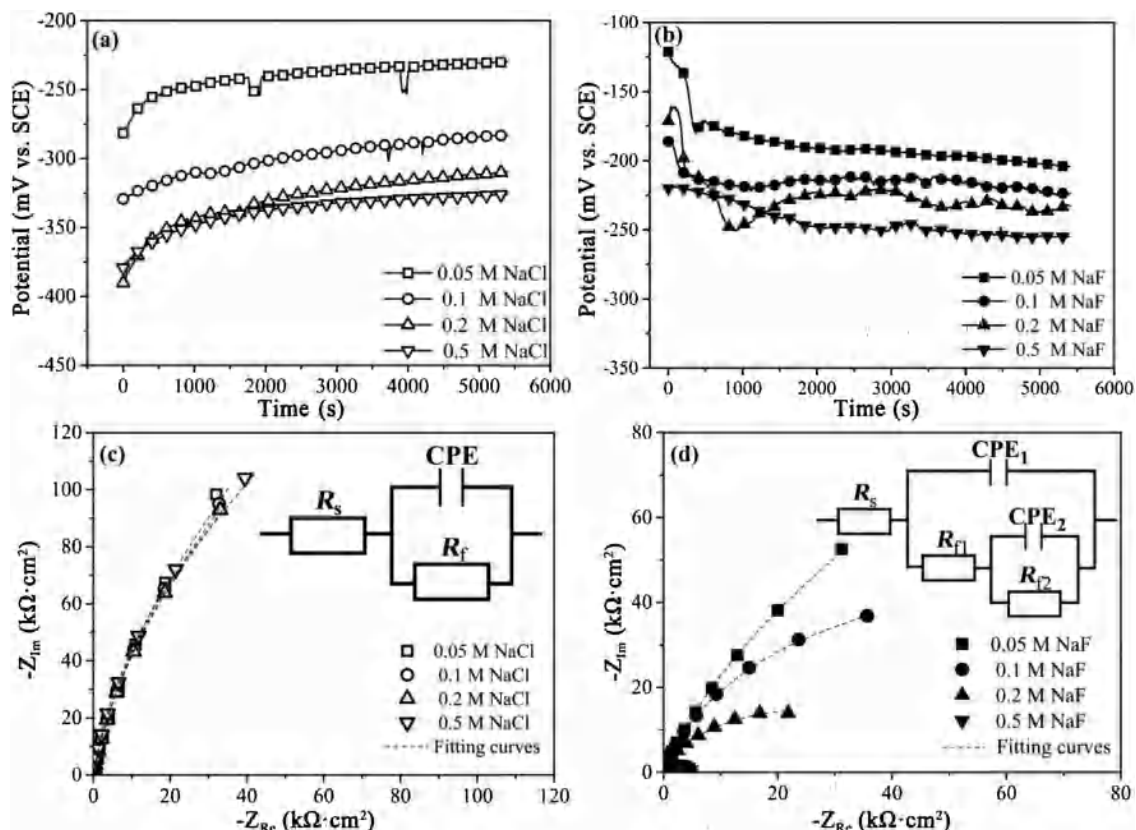
Fig. 2. Variations of open circuit potentials with time for $Zr_{52}Al_{10}Ni_6Cu_{32}$ metallic glass in electrolytes: (a) NaCl solutions; (b) NaF solutions, and the results of subsequent EIS tests with equivalent circuit used to fit data: (c) NaCl solutions; (d) NaF solutions.

Table 1
Values of impedance parameters of EIS experiments obtained by fitting for Zr-based metallic glass after open circuit potential tests.

NaCl Solution	R_s (Ω cm^2)	CPE (μS s^n cm^{-2})	n	R_f (kΩ cm^2)	R_p (kΩ cm^2)	χ^2 ($\times 10^{-4}$)
0.05 M	2.66	13.61	0.91	556.4	556.4	2.18
0.1 M	2.66	14.13	0.91	508.2	508.2	2.38
0.2 M	2.26	14.51	0.9	483.3	483.3	1.24
0.5 M	2.38	12.77	0.93	428.7	428.7	1.76

| NaF Solution	R_s (Ω cm^2)	CPE$_1$ (μS s^n cm^{-2})	n_1	R_{f1} (kΩ cm^2)	CPE$_2$ (μS s^n cm^{-2})	n_2	R_{f2} (kΩ cm^2)	R_p (kΩ cm^2)	χ^2
0.05 M	13.34	14.32	0.91	28.1	10.02	0.91	141.1	170.2	6.77
0.1 M	12.59	14.05	0.93	20.4	10.61	0.93	64.1	84.5	8.42
0.2 M	7.65	15.54	0.93	10.7	28.37	0.81	27	37.7	9.79
0.5 M	5.01	27.33	0.93	1.2	31.69	0.81	3.7	4.9	9.54

Table 2
Electrochemical parameters obtained from the polarization curves of $Zr_{52}Al_{10}Ni_6Cu_{32}$ BMG samples in NaCl and NaF solution.

|	NaCl			NaF		
	E_{corr} (mV vs SCE)	E_{pit} (mV vs SCE)	i_{corr} (μA/cm^2)	E_{corr} (mV vs SCE)	E_b (mV vs SCE)	i_{corr} (μA/cm^2)
0.05 M	-257 ± 28	-19 ± 59	164 ± 14	-184 ± 46	529 ± 74	168.6 ± 21
0.1 M	-291 ± 43	-46 ± 53	169 ± 8	-225 ± 29	243 ± 61	292.1 ± 19
0.2 M	-317.3 ± 19	-139 ± 30	178 ± 15	-249 ± 34	-40.0 ± 41	383.9 ± 60
0.5 M	-332.9 ± 33	-204 ± 59	201 ± 38	-289 ± 26	-149.8 ± 57	732.2 ± 116

and B. The corrosion pits are all in approximately rounded shapes and scattered randomly on the surface. Scratches due to polishing are visible on the surface, indicating that areas out of pits are undamaged. The compositions inside and outside of corrosion pits were compared by EDS analysis. Outside the pit, the alloy composition is almost identical to the nominal composition (see Fig. 5(c)). In contrast, the higher concentration of Cu and the existence of Cl, along with the reduction of Zr and Al content are observed in corrosion pit (Fig. 5(d)). This is due to the selective dissolution of Zr

and Al, which is consistent with the results commonly reported in the literature [18–20,49]. It is generally accepted that Cu can locally interact with Cl$^-$ to form CuCl, and subsequently CuO/Cu$_2$O is formed through hydrolysis [18,20,40,50].

Compared to the corrosion behaviours in NaCl environment, the situation in NaF solution is found to be quite different. The optical micrographs of the whole process of film destruction of $Zr_{52}Al_{10}Ni_6Cu_{32}$ BMG in 0.1 M NaF solution are shown in Fig. 6. The corresponding polarization curves for each stage are also provided
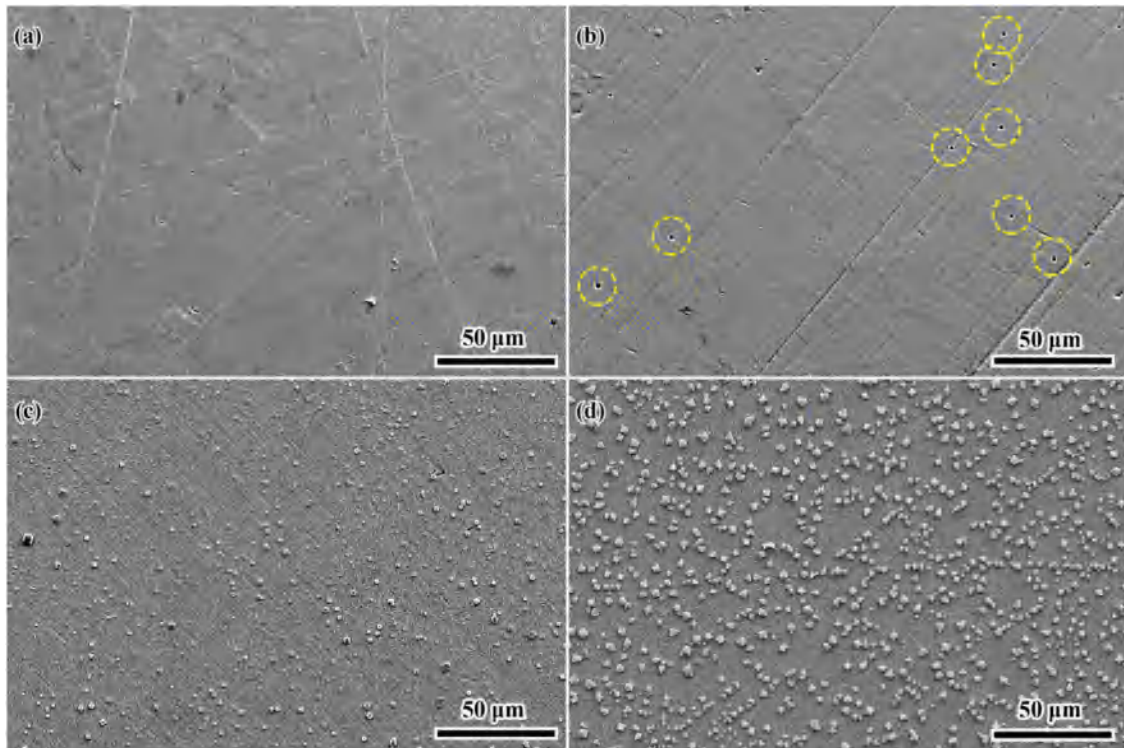
Fig. 3. Typical SEM images of $Zr_{52}Al_{10}Ni_6Cu_{32}$ metallic glass samples after open circuit potential tests in 0.2 M NaCl (a), 0.5 M NaCl (b), 0.2 M NaF (c), and 0.5 M NaF (d).
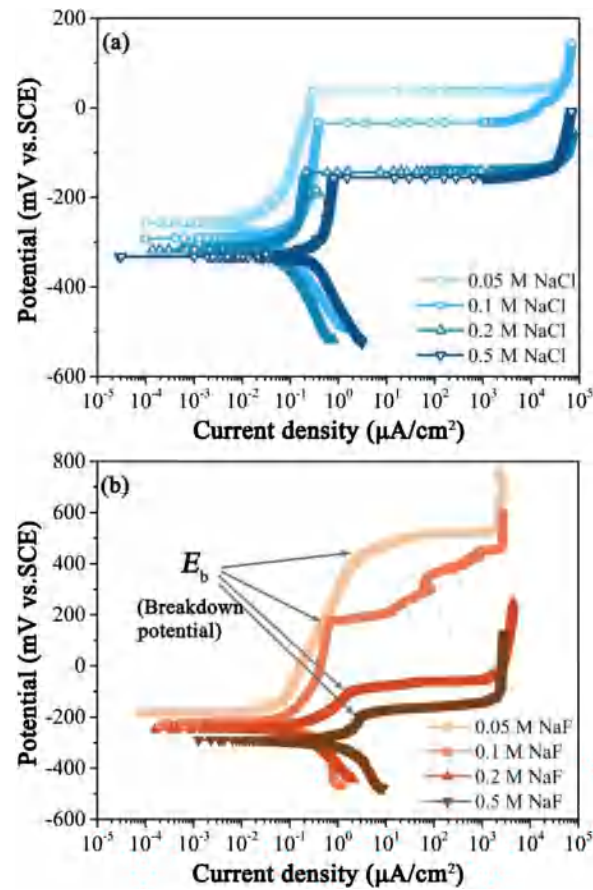
Fig. 4. Polarization behaviour of $Zr_{52}Al_{10}Ni_6Cu_{32}$ BMG samples obtained in NaCl (a) and NaF (b) solutions.
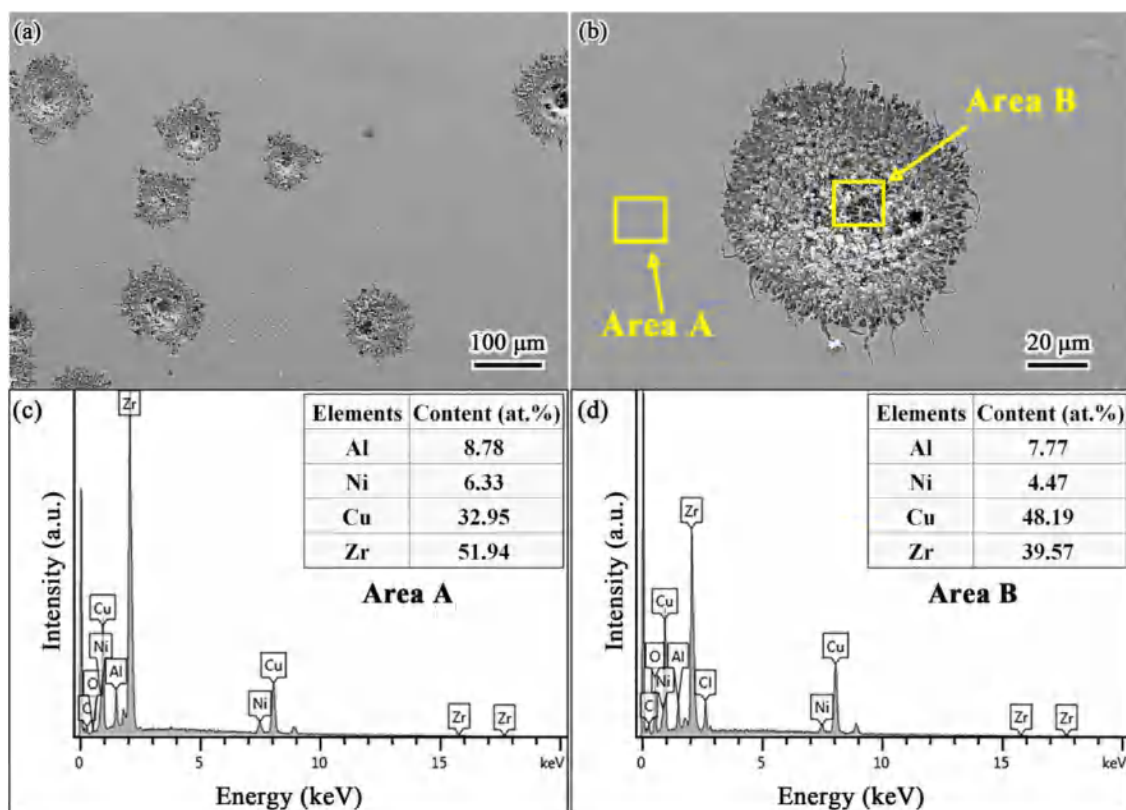
Fig. 5. Typical SEM images and corresponding EDS results of selected areas in $Zr_{52}Al_{10}Ni_6Cu_{32}$ BMG sample after pitting in 0.1 M NaCl solution: (a) Image of corroded surface; (b) High-resolution image of corrosion pit; (c) EDS results of area A; (d) EDS resuls of area B.
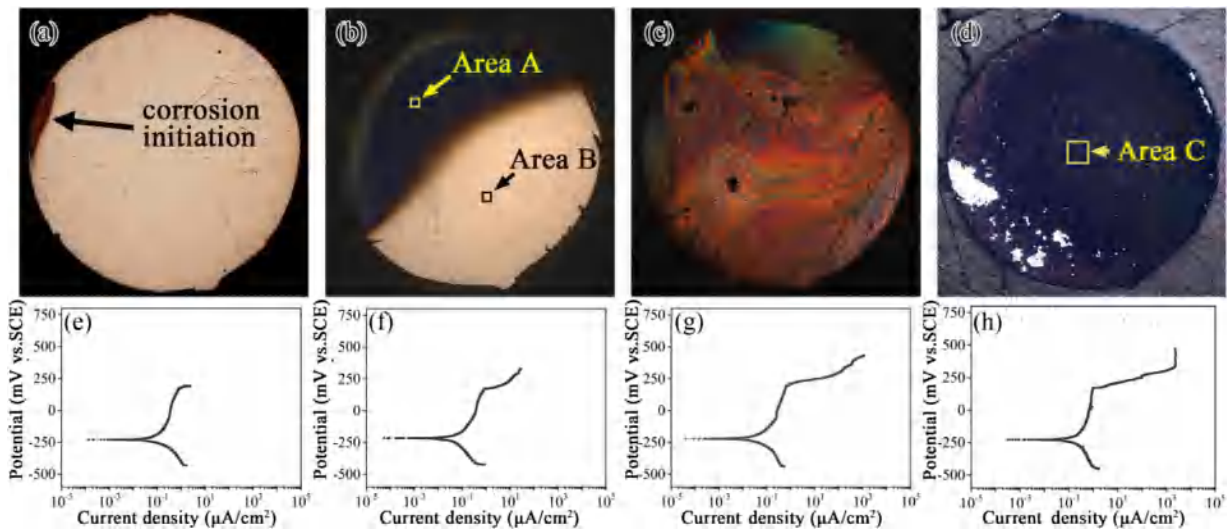
Fig. 6. Optical micrographs of polarization process of $Zr_{52}Al_{10}Ni_6Cu_{32}$ BMG samples in 0.1 M NaF solution: (a–d) and corresponding polarization curves (e–h).

in the figure. It should be pointed out that these images were taken separately from samples with different degrees of polarization (not in-situ observation). From these pictures we can confirm that the breakdown mechanism is not pitting in NaF solution.

The initial stage of surface breakdown is shown in Fig. 6(a). A small region in the alloy surface close to the epoxy resin turns dark, which is unlike pitting, where the film breakdown occurs randomly anywhere on the alloy surface, we found it reproducible that the destruction of the passive film in NaF solution always started at the crevice between alloy and epoxy resin. This is similar to the crevice corrosion that occurs in a solution system containing Cl⁻,

where corrosion occurs preferentially in the crevices between the solid phases [51–53]. Since the alloy surface was finely polished, the alloy/epoxy interfaces became weak points in morphology. Accordingly, Fig. 6(e) shows a slight increase in current density. Fig. 6(b) shows the expansion of film destruction. The corresponding current density raise to about 10 μA/cm² (Fig. 6(f)). The initial dark area of the sample surface gradually expands to the rest uncorroded area, and finally covers entire surface of the alloy, as shown in Fig. 6(c). The current density increases by two orders of magnitude, and it reaches 1000 μA/cm² (Fig. 6(g)). The advance of the corrosion is accompanied by the appearance of granular corrosion
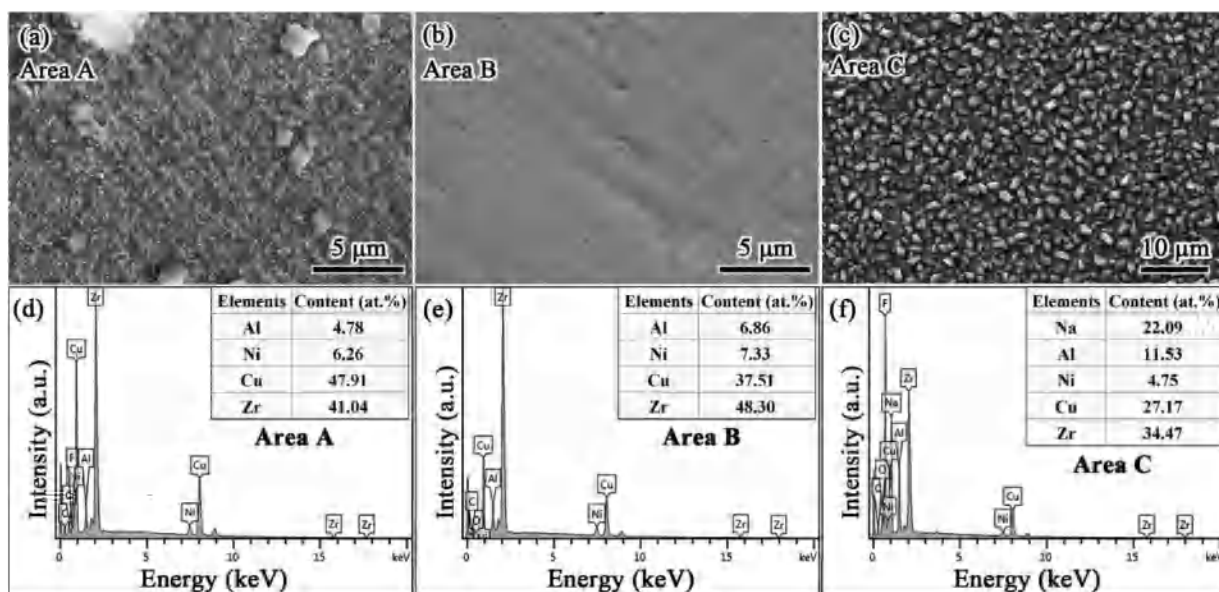
Fig. 7. High-resolution SEM images of the selected areas A, B and C in Fig. 6(a–c) and the corresponding EDS results (d–f).

products. When the whole alloy surface is damaged, as the potential shifts towards positive direction, the current gradually approaches a stable value (Fig. 6(h)), while the surface is gradually covered by a granular corrosion product layer, which is unstable and easy to be peeled off, as shown in Fig. 6(d).

Fig. 7 shows high-resolution SEM images of the highlighted area selected and corresponding EDS component results in Fig. 6. Fig. 7(a) shows area A in Fig. 6(b), which is the surface morphology after the breakdown of passive film. It can be seen that the scratches on the surface caused by polishing have disappeared, showing uniform corrosion morphology, along with the presence of granular corrosion products. EDS results shown in Fig. 7(d) indicate that Zr and Al are preferentially dissolved into the solution, leaving the surface enriched in Cu and Ni. F is also detected in this area. Fig. 7(b) shows the area where the surface film is not damaged, and scratches are still visible. EDS results in Fig. 7(e) suggest that the composition of this area is similar to the nominal composition and is not severely corroded. As shown in Fig. 7(c), after the surface film is completely destroyed, the formation of this corrosion product becomes the dominant reaction, and finally corrosion product covers the entire alloy surface. The EDS results in Fig. 7(f) show that the corrosion product is rich in Na, F, and Zr.

In order to confirm the corrosion product, XRD was used to characterize the corroded Zr-based BMG samples in NaF solution, the results are shown in Fig. 8. When we conduct XRD test on the sample shown in Fig. 6(d), only diffraction peaks with low intensity appeared at about $2\theta = 36°$. This indicates that the corrosion product only forms a very thin layer on the surface of the alloy and does not penetrate much into the alloy matrix. Therefore, we carried out further experiments. After the polarization process entered the diffusion-controlled region, the voltage was controlled at 800 mV vs. SCE and potentiostatically polarized for 3 h to obtain dense corrosion products. The pattern shows diffraction peaks superimposed on the broad diffuse halo from the amorphous phase. Sodium zirconium fluoride, i.e., Na_3ZrF_7, is confirmed. This corrosion product was previously found for pure Zr immersed in acidulated phosphate fluoride (APF) solutions of pH 5.0 [54]. From the above results, the corrosion of amorphous alloy in NaF solution seems to be dominated by the adsorption of F^-.

To further investigate the absorption of cations on alloy surface after passive film breakdown, XPS tests were conducted after polar-
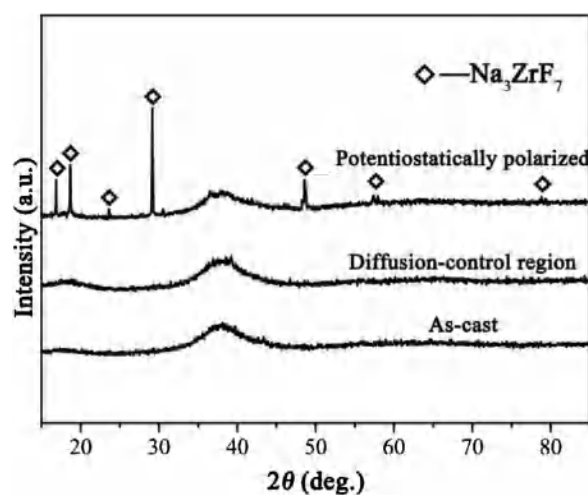

Fig. 8. XRD patterns of $Zr_{52}Al_{10}Ni_6Cu_{32}$ BMG samples obtained by different processing methods.

ization into diffusion-controlled region in both solutions (without maintaining voltage at 800 mV vs OCP). The results are shown in Figs. 9 and 10. As can be seen in Fig. 9, the peak of F 1s is detected after polarization in NaF solution, which proves the uniform adsorption of F^- on the alloy surface. However, in NaCl solution, Cl 2p is not detected. By comparing with EDS results in Fig. 5(d), it is proved that Cl^- only exists in corrosion pits, not the entire alloy surface. Furthermore, the high resolution XPS spectra in Fig. 10 show two peaks by multiplet splitting, Zr $3d_{3/2}$ and Zr $3d_{5/2}$. In Fig. 10(a), The peaks at 187.3 eV and at 184.8 eV were assigned to Zr^{4+} $3d_{3/2}$ and Zr^{4+} $3d_{5/2}$ electrons originating from the Na_3ZrF_7, which is in line with the values provided by Rakhmatullin [55]. In Fig. 10(b), the peaks obtained at 184.7 eV and 182.2 eV correspond to Zr^{4+} $3d_{3/2}$ and Zr^{4+} $3d_{5/2}$ electrons in ZrO_2 [56]. Thus, it can be concluded that in NaCl solutions Zr-based metallic glass forms a normal ZrO_2 passive film, whereas in NaF solutions ZrO_2 film is replaced by corrosion product Na_3ZrF_7.
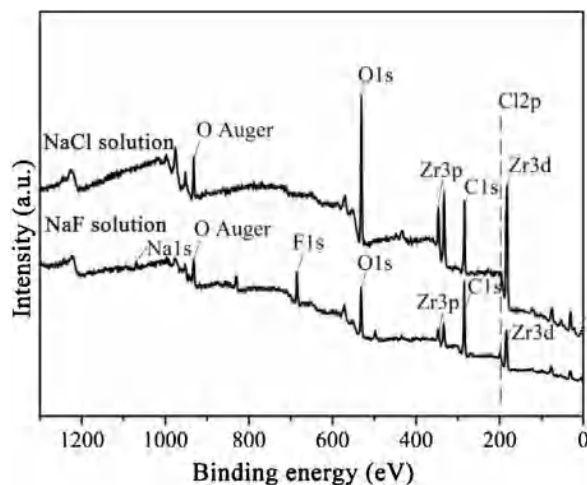
Fig. 9. XPS survey spectra of $Zr_{52}Al_{10}Ni_6Cu_{32}$ BMG samples after polarization into diffusion-controlled region in 0.1 M NaCl/NaF solution.
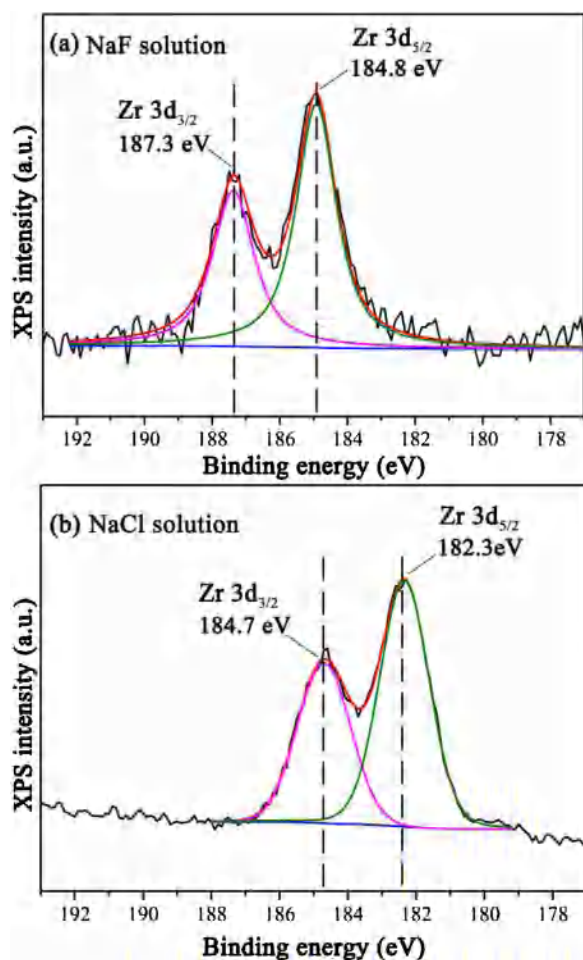

Fig. 10. High resolution XPS spectra of Zr 3d in Fig. 9.

4. Discussion

Above experimental results disclose that $Zr_{52}Al_{10}Ni_6Cu_{32}$ BMGs have completely different corrosion behaviours in NaF and NaCl solutions. The reasons are discussed from the following aspects.

Table 3
Ionic radii, surface charge densities, and viscosity B coefficients of ions.

	Ionic radii (nm)[a]	Surface charge density (mC/m²)	$B((L/mol)$[b]
F⁻	0.133	720.16	0.1
Cl⁻	0.181	388.84	−0.007
OH⁻	0.133	720.16	–
Zr⁴⁺	0.072	9824.67	–
Na⁺	0.102	1223.84	0.086

[a] From Ref. [57].
[b] From Ref. [58].

4.1. Initiation of passive film breakdown

During polarization stage, the pitting initiation in NaCl solution requires some time to be triggered, i.e., an approximately constant current density in passive region. However, the passive region is somewhat obscure in NaF solution, and it is replaced by a continuous and slow ascent (see Fig. 4). With the potential scanning upward, anions like Cl⁻ and OH⁻ migrate to the anode electrode then adsorb on the passive film. At the periphery of Cl⁻, water molecules are adsorbed by electrostatic forces. This electrostatic effect is even stronger for F⁻. According to the literature [36], the binding ability of the anion to surrounding water molecules can be characterized by viscosity coefficient B in Jones–Dole relationship.

$$\frac{\eta}{\eta_w} = 1 + A \times \sqrt{c} + B \times c \tag{2}$$

where η denotes the viscosity of the solution containing salt with concentration of c ; η_w denotes the viscosity of pure water. Coefficient A is always positive. When coefficient $B > 0$, the water layer is tightly attracted around the anion, so the flow of molecules in the solution will be subjected to greater resistance, thus the value of η is greater than that of pure water. On the other hand, when $B < 0$, water molecules are loosely accumulated around the anion, causing the viscosity to be similar to pure water. Table 3 lists some key physical properties of ions involved in the corrosion process.

Recently, by using aberration-corrected transmission electron microscopy, Zhang et al. [59] provided experimental evidence of the chloride ion accumulation at the metal/film interface, which results in lattice distortion at the interface. Although the direct destruction of the passive film was not observed in their experiment, it is predictable that such distortion will eventually lead to the destruction of the passive film. Analogously, the reactions occurring in the polarization process of $Zr_{52}Al_{10}Ni_6Cu_{32}$ BMG in NaCl solution mainly include:

$$Zr^{4+} + 2H_2O = ZrO_2 + 4H^+ \tag{3}$$

$$Zr^{4+} + Cl^- = ZrCl_4 \tag{4}$$

Reactions (3) and (4) refers to the formation of passive film and coordination process of Zr^{4+} and Cl^-, respectively. With $B < 0$, it is reasonable to speculate that when adsorbed on the passive film, Cl⁻ ions can easily lose the water molecular shell and enter the interior. Cl⁻ has a larger ion radius and can occupy the positions of metal elements. The accumulation of Cl⁻ gradually distorts metal/film interface, and eventually leads to the interface expansion. Fig. 11(a) shows the schematic diagram of the occurrence of the pitting. On the contrary, with $B > 0$, F⁻ is blocked outside because the water molecular shell tightly wraps around the periphery. The inability to pass through the passive film will lead to the accumulation of F⁻ on alloy surface. Therefore, when Zr^{4+}, Al^{3+} are dissolved from the matrix under the action of electric field, it will encounter F⁻ ion on the outside of the film. Predictably, F⁻ ion will shed its surrounding water shell and bind more tightly to Zr^{4+} due to its tiny ion radius and extremely high surface charge density (see Table 3). Due to the high surface charge density and small ion radius of Na⁺, it can
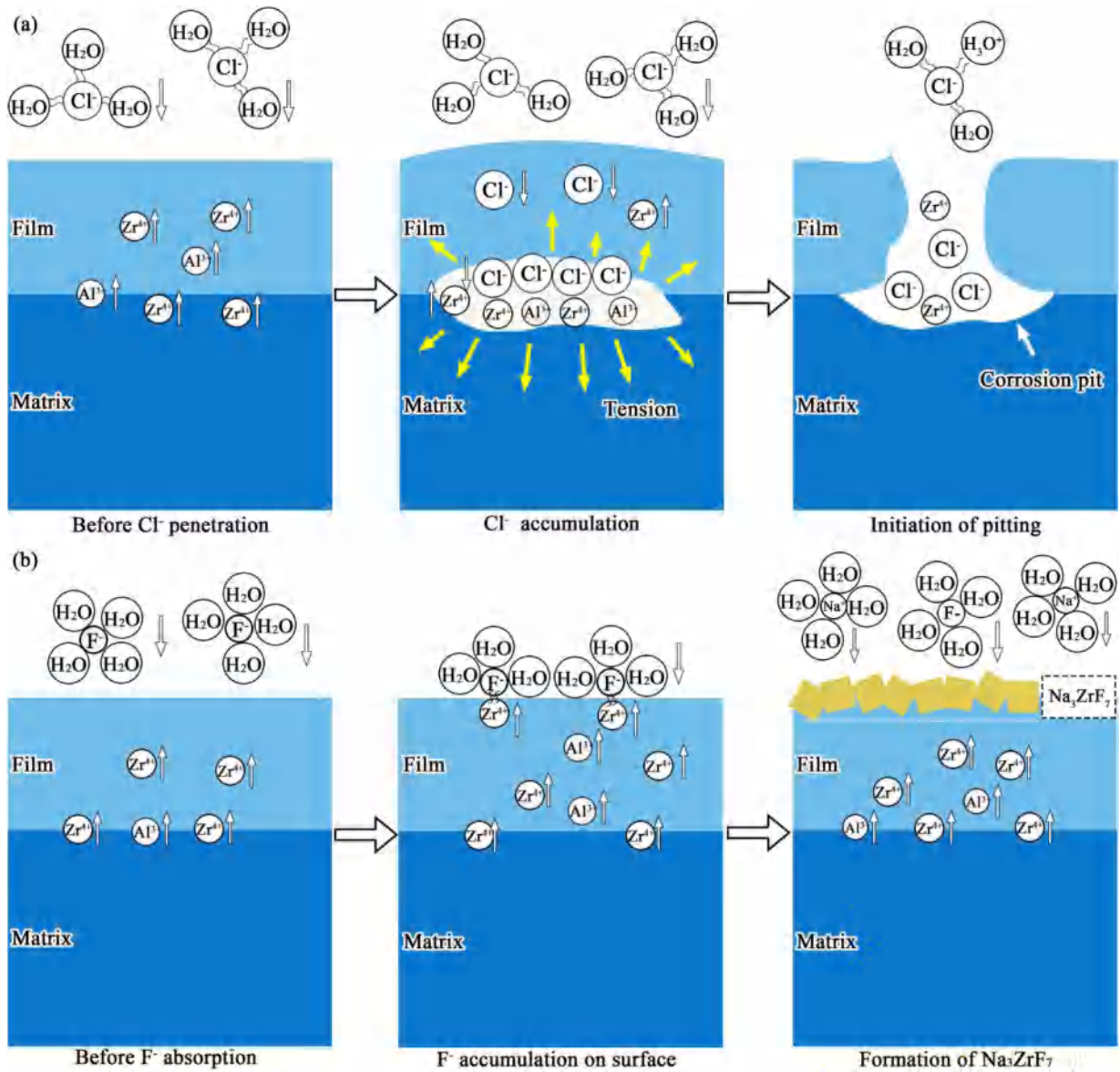
Fig. 11. Mechanism diagrams of amorphous alloy corrosion in NaCl (a) and NaF (b) solutions.

Table 4
Cumulative formation constants of zirconium cation with chloride, fluoride and hydroxide.

	$\log \beta_1$	$\log \beta_2$	$\log \beta_3$	$\log \beta_4$
Chloride[a]	0.9	1.3	1.5	1.2
Fluoride[b]	5.84	10.23	13.12	15.30
Hydroxide[a]	14.3	28.3	41.9	55.3

[a] From Ref. [60].
[b] From Ref. [61].

be inferred that Na$^+$ and F$^-$ are also closely bound in the solution. Therefore, it is reasonable to infer that the following reaction may be the cause of formation of Na$_3$ZrF$_7$.

$$3Na^+ + 7F^- + Zr^{4+} = Na_3ZrF_7 \qquad (5)$$

The formation constants provide the information of the strength of the interaction between cations and anions. The cumulative formation constants shown in Table 4 also suggest that the combination of Zr^{4+} is stronger with F$^-$ than with Cl$^-$. It should be pointed out that cumulative formation constant in Table 4 shows that OH$^-$ and Zr^{4+} have stronger binding force. However, considering that the pH of the solution is 7.0, the concentration of F$^-$ is much higher than that of OH$^-$, so the coordination of OH$^-$ and Zr^{4+} is negligible. At the same time, the coordination of Al^{3+} with anions can also be ignored due to its low content. A schematic diagram of the corrosion process in F- ion environment is shown in Fig. 11(b).

4.2. Preferential sites for breakdown initiation

As mentioned in earlier, the breakdown of passive film in NaF solution always occurs at the gap between the alloy and the epoxy resin, whereas the pitting in NaCl solution occurs randomly on alloy surface (see Figs. 5 and 6). We speculate that the key point of the distinction in corrosion mechanism is whether the anions pass through the passive film at weak points or uniformly adsorb on it. The passive film is not always complete and uniform. According to the literature [59], the prior pass of Cl$^-$ diffusion and transport in passive film is the grain boundaries between nanocrystals and amorphous phase. It is also known that Cl$^-$ ions preferentially attack secondary phases, impurities, or dislocations where pas-

sive film is not protective and unstable [62–64]. Channels provided by defects facilitate the transport and accumulation of Cl^-, which induces subsequent pitting corrosion. Thus, the gap between alloy and epoxy resin has no obvious advantage in pitting corrosion.

Compared to the selective accumulation of Cl^- at defects, F^- ions are more inclined to evenly adsorb on passive film, therefore the role of defects providing channels for ion transport is less important in this case.

One possible mechanism is that uniform dissolution of Zr^{4+} on a surface away from the crevice leads to uniform adsorption of F^-. However, the mass transfer of Zr^{4+} is hindered in the crevice between alloy/epoxy.

Meanwhile, the hydrolysis of Zr^{4+} (Eq. (3)) leads to a decrease in pH, these cations are difficult to diffuse out of the crevice. Therefore, in order to keep the solution electrically neutral, more F^- are attracted to the crevice, prompting the formation of Zr/F compounds more rapidly.

4.3. Expansion of corrosive surface

After pitting initiating in Cl^--containing electrolytes, the area of corrosion pits can increase sharply. The depletion of less noble elements Zr/Al and the enrichment of Cu in corrosion pits give rise to the formation of galvanic cells where pits act as cathodes and uncorroded areas act as anode [19]. Within the limited experimental time, pits do get a chance to grow too large. However, limited defect points prevent the tendency of pitting expansion towards the entire surface.

However, the situation is completely different in F- containing solution. Due to the uniform adsorption of F^- on passive film, the corrosion progression is approximately the same anywhere on alloy surface, which makes the breakdown of the passive film on the uncorroded surface triggered easily. In this case, the enrichment of noble element Cu on damaged surface is also evident. During the expansion process of the film breakdown, the damaged surface acting as the cathode accelerates the anodic reaction on the undamaged surface. This iterative and incremental reaction eventually causes the entire passive film to be destroyed. It is well acknowledged that crystalline phase in glassy matrix also act as cathode [21,65], thus we suggest that Na_3ZrF_7 can couple with the surrounding uncorroded surface to cause galvanic corrosion, thereby accelerating corrosion on the surrounding surface. During upward scanning, the formation rate of Na_3ZrF_7 is higher than its dissolution rate. A layer of Na_3ZrF_7 replaces the passive film and finally covers the entire surface, resulting in diffusion control.

5. Conclusions

In this paper, the corrosion behaviours of $Zr_{52}Al_{10}Ni_6Cu_{32}$ BMG alloys in NaCl and NaF solutions were investigated. The potential corrosion mechanisms of Zr-based BMG in Cl^- and F^- environments were proposed. The main findings can be summarized as follows:

(1) In the OCP tests, the potential of the $Zr_{52}Al_{10}Ni_6Cu_{32}$ BMG samples increases with time in NaCl solution, while the opposite trend is shown in NaF solution.
(2) In the process of upward polarization $Zr_{52}Al_{10}Ni_6Cu_{32}$ BMG material exhibits completely different corrosion behaviours in NaCl and NaF solutions, i.e., pitting corrosion in Cl^- environment and uniform corrosion in F^- environment. Furthermore, in uniform corrosion the passive film breakdown initiates in the crevices between the alloy surface and the epoxy resin, and then spreads to the whole surface.
(3) The distinct corrosion behaviour of $Zr_{52}Al_{10}Ni_6Cu_{32}$ BMG material in NaCl solution and NaF solution can be interpreted in

terms of the differences in binding ability of anions to surrounding molecules. With loose molecule bonding Cl^- can pass through the passive film and accumulate at metal/film interface, which results in lattice distortion and subsequent pitting corrosion. In contrast, F^- is unable to penetrate the passive film due to strong combination with water molecules, which causes a large number of F^- to be adsorbed on the outside of the film and coordinate with Zr^{4+}. This process induces the formation of a dense layer of Na_3ZrF_7 on the surface of the alloy, which slows the anodic process.

References

[1] W.H. Wang, C. Dong, C.H. Shek, Mater. Sci. Eng. R-Rep. 44 (2004) 45–89.
[2] A. Inoue, A. Takeuchi, Acta Mater. 59 (2011) 2243–2267.
[3] J.C. Qiao, J.M. Pelletier, J. Mater. Sci. Technol. 30 (2014) 523–545.
[4] Z.F. Zhang, F.F. Wu, G. He, J. Mater. Sci. Technol. 23 (2007) 747–767.
[5] M. Iqbal, J.I. Akhter, H.F. Zhang, Z.Q. Ho, J. Mater. Sci. Technol. 23 (2007) 693–696.
[6] Q.P. Cao, J.B. Jin, Q. Yu, X.D. Wang, D.X. Zhang, Y. Jiang, J.Z. Jiang, J. Mater. Sci. Technol. 30 (2014) 595–598.
[7] W. Zhou, W.P. Weng, J.X. Hou, J. Mater. Sci. Technol. 32 (2016) 349–354.
[8] Y.J. Li, Y.G. Wang, B. An, H. Xu, Y. Liu, L.C. Zhang, H.Y. Ma, W.M. Wang, PLoS One 11 (2016), e0146421.
[9] S.X. Liang, Z. Jia, Y.J. Liu, W. Zhang, W. Wang, J. Lu, L.C. Zhang, Adv. Mater. 30 (2018), 1802764.
[10] L.C. Zhang, Z. Jia, F. Lyu, S.X. Liang, J. Lu, Prog. Mater. Sci. 105 (2019), 100576.
[11] J.R. Scully, A. Gebert, J.H. Payer, J. Mater. Res. 22 (2007) 302–313.
[12] A. Inoue, X.M. Wang, W. Zhang, Rev. Adv. Mater. Sci. 18 (2008) 1–9.
[13] A. Gebert, K. Mummert, J. Eckert, L. Schultz, A. Inoue, Mater. Corros. 48 (1997) 293–297.
[14] W.H. Peter, R.A. Buchanan, C.T. Liu, P.K. Liaw, M.L. Morrison, J.A. Horton, C.A. Carmichael, J.L. Wright, Intermetallics 10 (2002) 1157–1162.
[15] U.K. Mudali, S. Scudino, U. Kuhn, J. Eckert, A. Gebert, Scr. Mater. 50 (2004) 1379–1384.
[16] A. Gebert, K. Buchholz, A. Leonhard, K. Mummert, J. Eckert, L. Schultz, Mater. Sci. Eng. A 267 (1999) 294–300.
[17] S. Baunack, U.K. Mudali, A. Gebert, Appl. Surf. Sci. 252 (2005) 162–166.
[18] B.A. Green, H.M. Meyer, R.S. Benson, Y. Yokoyama, P.K. Liaw, C.T. Liu, Corros. Sci. 50 (2008) 1825–1832.
[19] K. Mondal, B.S. Murty, U.K. Chatterjee, Corros. Sci. 48 (2006) 2212–2225.
[20] A. Kawashima, K. Ohmura, Y. Yokoyama, A. Inoue, Corros. Sci. 53 (2011) 2778–2784.
[21] U.K. Mudali, S. Baunack, J. Eckert, L. Schultz, A. Gebert, J. Alloys Compd. 377 (2004) 290–297.
[22] V.R. Raju, U. Kuhn, U. Wolff, F. Schneider, J. Eckert, R. Reiche, A. Gebert, Mater. Lett. 57 (2002) 173–177.
[23] S.J. Pang, T. Zhang, K. Asami, A. Inoue, J. Mater. Res. 18 (2003) 1652–1658.
[24] X.P. Nie, X.M. Xu, Q.K. Jiang, L.Y. Chen, Y. Xu, Y.Z. Fang, G.Q. Xie, M.F. Luo, F.M. Wu, X.D. Wang, Q.P. Cao, J.Z. Jiang, J. Non-Cryst. Solids 355 (2009) 203–207.
[25] F.X. Qin, X.M. Wang, G.Q. Xie, K. Wada, M. Song, K. Furuya, K. Asami, A. Inoue, Intermetallics 17 (2009) 945–950.
[26] C. Qi, L. Lin, Z. Sheng-Min, Front. Mater. Sci. China 4 (2010) 34–44.
[27] H.F. Li, Y.F. Zheng, Acta Biomater. 36 (2016) 1–20.
[28] J. Paillier, C. Mickel, P.F. Gostin, A. Gebert, Mater. Charact. 61 (2010) 1000–1008.
[29] U. Wolff, A. Gebert, J. Eckert, L. Schultz, J. Alloys Compd. 346 (2002) 222–229.
[30] M. Zhou, X. Huang, K. Hagos, Y.W. Cui, L.Q. Ma, Intermetallics 90 (2017) 23–29.
[31] G.A. EL-Mahdy, S.S. Mahmoud, H.A. El-Dahan, Thin Solid Films 286 (1996) 289–294.
[32] A.A. Ghoneim, Mater. Corros. 55 (2004) 617–622.
[33] Y.H. Duan, P. Li, M. Zhang, M.J. Peng, L.S. Ma, B.P. Shu, J. Alloys Compd. 729 (2017) 1108–1117.
[34] D. Davies, R. Prigmore, Br. Corros. J. 21 (1986) 191–194.
[35] J.L. Trompette, L. Massot, L. Arurault, S. Fontorbes, Corros. Sci. 53 (2011) 1262–1268.
[36] J.L. Trompette, Corros. Sci. 82 (2014) 108–114.
[37] J.L. Trompette, Corros. Sci. 94 (2015) 288–293.

[38] J.L. Trompette, L. Arurault, S. Fontorbes, L. Massot, Electrochim. Acta 55 (2010) 2901–2910.
[39] W.T. Tsai, J.T. Chen, Corros. Sci. 49 (2007) 3659–3668.
[40] A. Gebert, P.F. Gostin, L. Schultz, Corros. Sci. 52 (2010) 1711–1720.
[41] H. Tanimoto, Y. Soga, Y. Takayanagi, H. Mizubayashi, Mater. Trans. 52 (2011) 1402–1409.
[42] J.R. Macdonald, Solid State Ionics 13 (1984) 147–149.
[43] K. Jüttner, Electrochim. Acta 35 (1990) 1501–1508.
[44] J. Tang, L. Yu, J. Qiao, Y. Wang, H. Wang, M. Duan, M. Chamas, Electrochim. Acta 267 (2018) 222–233.
[45] N.D. Nam, J.G. Kim, Corros. Sci. 52 (2010) 3377–3384.
[46] J.R. Macdonald, E. Barsoukov, Impedance Spectroscopy: Theory, Experiment, and Applications, History, 1, Wiley Interscience, 2005, pp. 1–13.
[47] J. Soltis, Corros. Sci. 90 (2015) 5–22.
[48] D.D. Macdonald, Corros. Eng. Sci. Technol. 49 (2014) 143–155.
[49] Y. Li, J. Xu, Corros. Sci. 128 (2017) 73–84.
[50] Y. Zhang, L. Yan, X. Zhao, L. Ma, J. Non-Cryst. Solids 496 (2018) 18–23.
[51] J.C. Griess, Corrosion 24 (1968) 96–109.
[52] R.B. Diegle, Corrosion 36 (1980) 362–368.
[53] S.M. Sharland, Corros. Sci. 27 (1987) 289–323.
[54] Ki. Yokoyama, D. Yamada, Ji. Sakai, Corros. Sci. 73 (2013) 375–381.
[55] A. Rakhmatullin, M. Boča, J. Mlynáriková, E. Hadzimová, Z. Vasková, I.B. Polovov, M. Mičušík, J. Fluorine Chem. 208 (2018) 24–35.
[56] C.D. Wanger, W.M. Riggs, L.E. Davis, J.F. Moulder, G.E. Muilenberg, Handbook of X-ray Photoelectron Spectroscopy, Perkin-Elmer Corp., Physical Electronics Division, Eden Prairie, Minnesota, USA, 1979, pp. 100–101.
[57] Y. Marcus, J. Chem, Soc. Faraday Trans. 87 (1991) 2995–2999.
[58] K.D. Collins, Methods 34 (2004) 300–311.
[59] B. Zhang, J. Wang, B. Wu, X. Guo, Y. Wang, D. Chen, Y. Zhang, K. Du, E. Oguzie, X. Ma, Nat. Commun. 9 (2018) 2559.
[60] J.A. Dean, Lange's Handbook of Chemistry, McGraw-Hill, Inc., New york, London, 1999.
[61] S.U. Aja, S.A. Wood, A.E. Williams-Jones, Appl. Geochem. 10 (1995) 603–620.
[62] A. Gebert, P.F. Gostin, M. Uhlemann, J. Eckert, L. Schultz, Acta Mater. 60 (2012) 2300–2309.
[63] A. Kawashima, Y. Yokoyama, A. Inoue, Corros. Sci. 52 (2010) 2950–2957.
[64] A. Tauseef, N.H. Tariq, J.I. Akhter, B.A. Hasan, M. Mehmood, J. Alloys Compd. 493 (2010).
[65] A. Gebert, U. Kuehn, S. Baunack, N. Mattern, L. Schultz, Mater. Sci. Eng. A 415 (2006) 242–249.